



Experimental investigation of a keying joint cast in UHPFRC between precast UHPFRC bridge elements

Numa J. Bertola · Ngoc Thanh Trinh · Enrique Garcia · Eugen Brühwiler

Received: 21 December 2021 / Accepted: 27 February 2022
© The Author(s) 2022

Abstract Ultra High-Performance Fiber-Reinforced Cementitious Composite (UHPFRC) is increasingly popular for new structural designs thanks to its high resistance both in tension and compression. When UHPFRC is complemented with steel reinforcing bars or prestressing tendons, the structure remains waterproof and crack-free under service conditions, significantly improving the durability compared to conventional reinforced-concrete designs. The Aiguillon Bridge is one of the first railway bridges entirely made of UHPFRC. Built in 2021 in Switzerland, this bridge has a single span of 6.6 m and a width of 5.4 m. The bridge is designed for a narrow track and 2 walkways. Two prefabricated elements in UHPFRC have been assembled on-site by a longitudinal cast-in-place UHPFRC keying joint. This paper presents the

full-scale laboratory experiment to validate the keying joint suitability for railway bridges. This experimental investigation involves a static test on a transverse beam composed of two precast elements and the keying joint. Results show that the structure presents a post-peak ductile behavior as well as an elastic behavior under service loads. Digital-Image-Correlation measurements provide details on the cracking patterns of the interface between the keying joint and the precast elements. As the maximum resistance obtained during the experiment is in agreement with the analytical-model predictions, the concept of the keying joint is validated.

Keywords Ultra-High Performance Fibre Reinforced Cementitious Composite, Structural UHPFRC · Railway bridge · Keying joint

N. J. Bertola (✉) · E. Brühwiler
Laboratory for Maintenance and Safety of Structures,
Ecole Polytechnique Fédérale de Lausanne (EPFL),
Station 18, 1015 Lausanne, Switzerland
e-mail: numa.bertola@epfl.ch

E. Brühwiler
e-mail: eugen.bruehwiler@epfl.ch

N. T. Trinh
Engineering Structure Department, Stucky Ltd, Renens,
Switzerland
e-mail: ngoc-thanh.trinh@stucky.ch

E. Garcia
TRAVYS Ltd, Yverdon-les-Bains, Switzerland
e-mail: e.garcia@travys.ch

1 Introduction

Reinforced concrete (RC) structures have been widely built around the world since the beginning of the 20th century. After years or decades, these structures often have durability issues, like rebar corrosion or alkali-aggregate reaction in concrete. These degradations can significantly reduce structural performance. Interventions to rehabilitate structures are thus of interest in most developed countries. However, the rehabilitation



of deteriorated structures typically has high intervention costs and indirect user costs [1]. Traditional retrofitting solutions using concrete and repair mortar are not durable enough, meaning that novel rehabilitation strategies of RC structures are needed that are effective, sustainable, and economic [2]. Another solution lies in improving structural systems using high-performance materials to simultaneously reduce intervention costs and duration as well as improve structural durability [3].

Among these new high-performance materials, Ultra-High-Performance Fibre Reinforced Cementitious Composite (UHPFRC) has been used in structures worldwide for twenty years [4, 5]. UHPFRC is made of a mix of cement, fine hard particles (with a maximum grain size of 1 mm), water, admixtures, additives, and a large amount of short slender steel fibers [6]. Steel fibers typically represent at least a 3-% volume of the material [7].

The mechanical properties of UHPFRC are summarized in [8, 9]. UHPFRC has significant mechanical strength, both in tension (up to 16 MPa) and compression (up to 150 MPa) (Fig. 1). The Young's modulus is around 45 GPa, and the material has a strain-hardening behavior until 1–2‰ in tension. The tensile strength can be significantly improved by adding reinforcement bars (R-UHPFRC), similar to RC structures [10]. Most of the research on R-UHPFRC has focused on the ultimate resistance [11–13], monotonic loading [14, 15] and under service conditions [16]. UHPFRC is material with specific properties and requires specific design codes and execution processes. In Switzerland, the Technical

Leaflet on UHPFRC (SIA 2052) [17] was introduced in 2016 to provide guidance on structural designs with UHPFRC.

Due to its strain-hardening behavior, UHPFRC typically remains free of discrete cracks under service conditions [18]. To guarantee this property, it is recommended in SIA 2052 to limit the maximum tensile strain of UHPFRC elements to 1‰ under service conditions, a criterion based on [19]. For engineering applications, UHPFRC is thus considered to be waterproof under service conditions, providing robust protection against environmental actions (water and chloride ion ingress) [20]. This waterproof property of UHPFRC has been validated using in-situ measurements of air permeability of UHPFRC layers cast on existing RC bridges several years after interventions in Switzerland [21] and for a new design in UHPFRC in France [22]. Due to its mechanical properties, UHPFRC structures have relatively slender elements and show reduced maintenance. Therefore, UHPFRC structures have shown significantly better durability performance than traditional RC structures for both new design [23] and structural strengthening [24].

Since the 1st intervention in 2004 [25], more than 300 projects have involved structural UHPFRC in Switzerland [26]. Despite this experience and structural codes, collaborations between academic and design offices are sometimes required for specific designs. This study presents the results of such collaboration on understanding the behavior of a transverse beam of a bridge project prior to its construction.

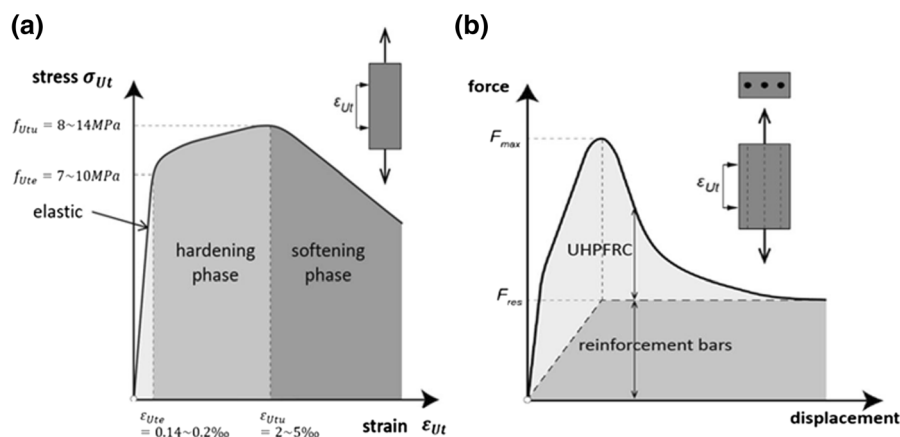


Fig. 1 Tensile properties **a** plain UHPFRC and **b** reinforced UHPFRC

Recent efforts in research aim to understand specific properties of UHPFRC better. The fiber orientation and distribution are of particular interest as this property can significantly affect the structural performance and permeability [19, 27]. These issues are typically addressed by including reduction factors on UHPFRC tensile strength [28, 29]. Another aspect is the fatigue resistance of UHPFRC elements on direct tensile tests of UHPFRC elements [30] and R-UHPFRC beams [31, 32]. As these studies mostly involved laboratory tests, several monitoring systems and non-destructive tests have been used and validated for UHPFRC elements. In the present study, the behavior of a UHPFRC element involving a keying joint is monitored based on the same instruments, such as digital image correlation (DIC), extensometers, and LVDT. The structural behavior of a UHPFRC beam involving keying joints is of interests due to the discontinuity of fiber within the structural element. Recently, it has been shown that wet joints reduce the flexural capacity of UHPFRC beams [33]. However, a comprehensive study of the collapse mechanism of UHPFRC beams with keying joints is missing.

This paper presents the experimental investigation of a keying-joint behavior between 2 precast elements, all made of UHPFRC. This laboratory experiment involves a full-scale static test of a transverse beam on one of the 1st railway bridges in UHPFRC. This study includes investigations on several aspects of the beam behavior: the force–displacement response, the cracking patterns, and the collapse mechanism.

The manuscript is organized as follows. Section 2 presents the experimental setup and the analytical models of the beam resistance. In Sect. 3, the results of the experimental campaign are shown. Eventually, an inverse analysis to obtain beam properties and steel-reinforcement stresses during the experiment is performed in Sect. 4.

2 Experimental investigations

2.1 Bridge presentation

The bridge was built in 2021 in a remote mountainous area. The present laboratory experiment was conducted as a suitability test to validate the design prior to the construction.

The structure has a single span of 6.6 m and a width of 5.4 m. The cross-section is a U-shape trough for ballast and involves one track lane and two pedestrian walkways on the sides. The deck thickness is 60 mm and is supported by several transverse squared beams with a depth of 180 mm spaced every 650 mm. The service speed of trains in this area is limited to 45 km/h, meaning that dynamic behavior is not critical and is not considered in this study.

Due to the difficulty of accessing the bridge location, the cross-section has been divided into three elements (Fig. 2). The contractor has prefabricated the 2 halves of the trough, and the keying joint was cast on-site. The transverse beams thus include 2 precast elements and a keying joint. This design leads to particular structural properties as the fibers are not continuous at the interfaces between the precast elements and the keying joint. Therefore, the tensile strength of UHPFRC is expected to be significantly lower at these interfaces. This study aims to investigate the behavior of this transverse beam through a full-scale experiment of a static test in the laboratory.

2.2 Test specimen

The manufacturer has prepared a transverse beam with the same cross-section as for the future bridge. The 2 precast elements were 1st prepared. Then, the keying joint was cast, and the element was transported to the laboratory 28 days later for the test. The beam length is slightly larger than on the bridge to apply loads in the laboratory with the same span as under the final bridge condition.

The beam has a total length of 3 m (Fig. 3). The cross-section includes the squared beam of 180 mm and 650 mm of the deck to replicate the T-shape behavior. Reinforcements of both precast elements intersect within the keying joint. In each precast element, this reinforcement involves 2 layers of 2 rebars with a diameter of 26 mm. These bars are bent to follow the shape of the keying joint, ensuring their anchorage. On the compressive side, each precast element has four rebars with a diameter of 16 mm.

UHPFRC properties are the same between precast elements and the keying joint (Table 1). Four UHPFRC properties are defined: The Young modulus E , the compressive strength $f_{U,c}$, the elastic limit stress $f_{U,le}$ and the tensile resistance $f_{U,tu}$. Both elements

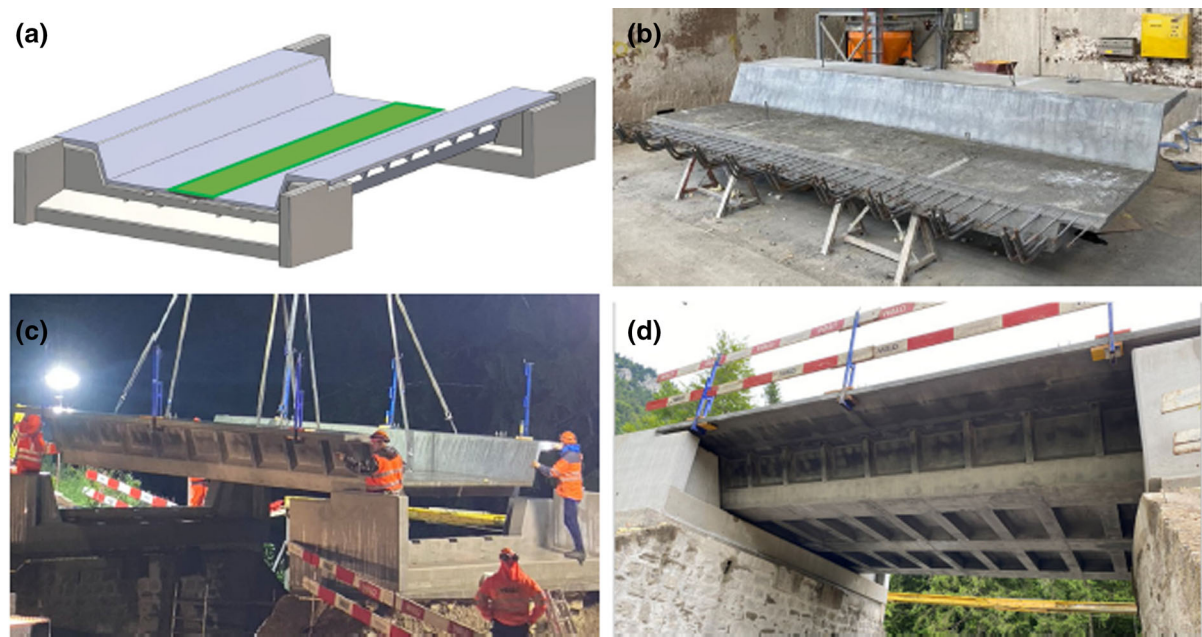


Fig. 2 Bridge presentation. **a** Model of the bridge with the keying joint in green and precast elements in blue; **b** first precast element at the contractor's shop; **c** installation of the UHPFRC trough; **d** bottom view of the trough after the installation

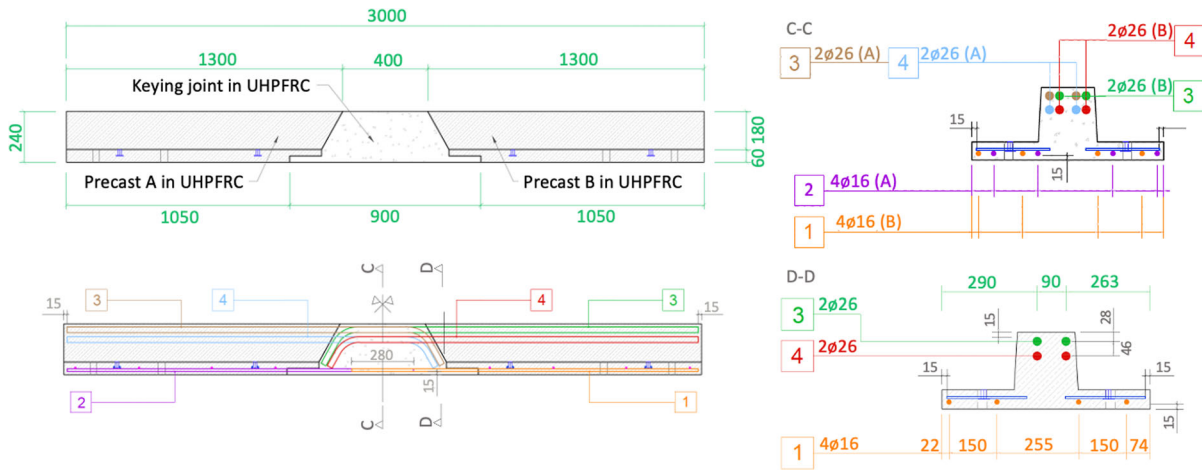


Fig. 3 Test-specimen characteristics

Table 1 Material properties (nominal values according to the selected sort of UHPFRC)

Element	E_U [MPa]	$f_{U,c}$ [MPa]	$f_{U,te}$ [MPa]	$f_{U,tu}$ [MPa]
<i>UHPFRC (UB)</i>				
Precast elements	45,000	180	10	12
Keying joint	45,000	180	10	12
<i>Steel reinforcement (B500B)</i>				
Material	E_s [MPa]	f_y [MPa]		
Steel	205,000	550		

(precast and poured) are made with the same premix, and they are expected to reach UHPFRC Type UB, the highest quality according to the technical leaflet [17]. All properties are taken as median values in order to have model predictions as close as possible to the observed behavior during the experiment. Two steel properties are defined: the Young's modulus E_s and the yield strength f_y .

2.3 Analytical model of beam bending resistance

In this section, the analytical model of the beam bending resistance is presented. This model is taken from the technical leaflet for R-UHPFRC [17]. This model involves the hypothesis of a plastic behavior of

the materials. Three cross-sections are analyzed (Fig. 4). Section A is at the midspan of the beam and involves reinforcement of both precast elements. Section B lies in the precast element. Section C is at the interface between the keying joint and the precast element. Due to the fiber discontinuity at this interface, the tensile strength of UHPFRC is not considered in the resistance model of this cross-section. These flexural-behavior models must be validated for this particular beam design, and it is one of the goals of this experimental study.

For each cross-section, the maximum force based on the analytical model is obtained (Table 2). Section C has the smallest value of maximal theoretical force ($Q_{\max,th} = 204kN$), while the maximal forces are

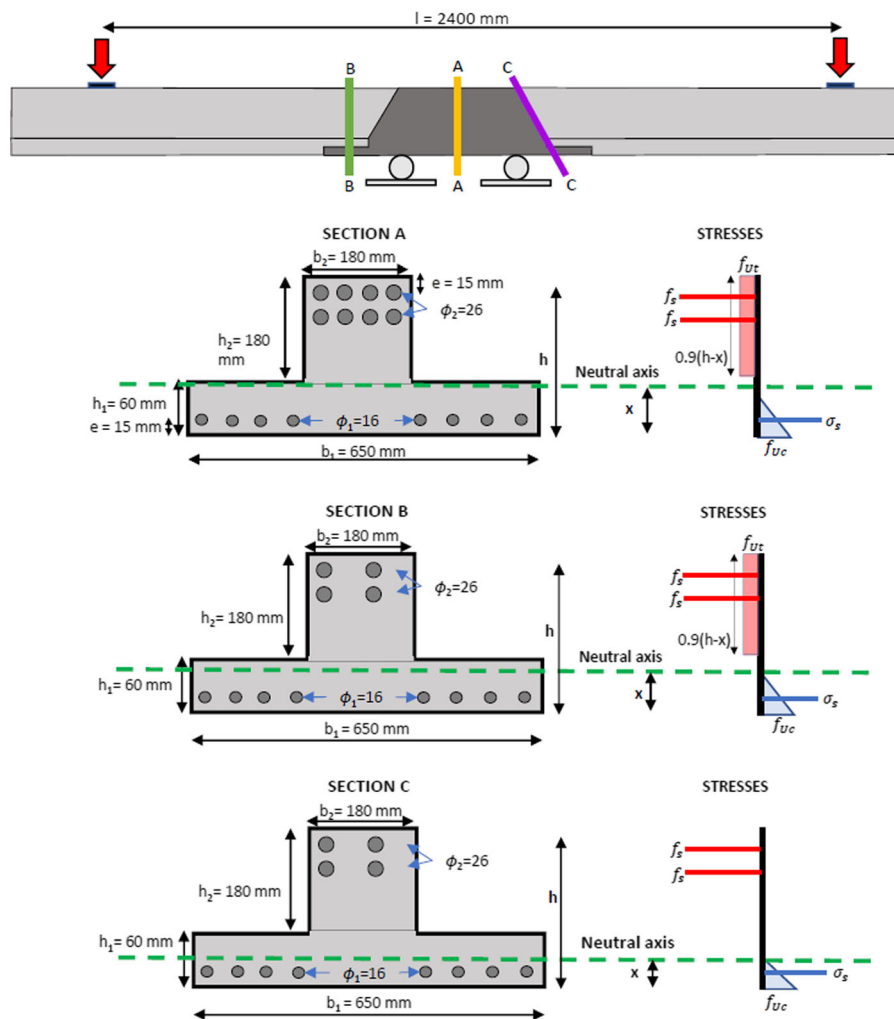


Fig. 4 Analytical resistance models of beam cross-sections

Table 2 Maximum force obtained using the analytical model for each cross-section

Maximal theoretical force	Section A	Section B	Section C
$Q_{\max,th}$ [kN]	470	310	204

significantly larger within the keying joint (Section A) and the precast element (Section B). This result means that the weakest section of the beam is at the interfaces between the precast element and the keying joint as no tensile strength of UHPFRC is obtained due to the absence of fibers at the interfaces of the joint.

3 Experimental results

3.1 Test setup and instrumentation

The measurement system set up for the tests is shown in Fig. 5. The beam deformation measurements were made using a Digital Image Correlation (DIC), thanks to 2 Manta 20MPix cameras. The measurement was done on an area of 1.4×0.24 m on the central area of the beam, including the keying joints on both sides, and measurements have a precision of at least 0.01 mm. Two LVDTs were installed under the actuators to measure the beam vertical displacement. Finally, 5 extensometers were installed. The first 3 are placed on top of the beam between the supports to have the maximum deformation. The 2 remaining sensors are installed above the joints on both sides to monitor the crack opening at the vertical level of the first layer of rebars.

Two hydraulic jacks (capacity of 1000 kN each) are used to apply a displacement on both sides of the beam. The experiment is controlled by an imposed linearly increasing or decreasing displacement with a speed of 0.02 mm/s. First, 5 loading–unloading cycles are performed between service and self-weight load levels of the actual transverse beam of the bridge trough to observe the beam behavior under service conditions. Then, the imposed displacement is increased until the beam exhibits significant deformation and either rebar yielding or debonding with large macrocracks. At this point, it can be assumed that the beam has collapsed (Fig. 5).

3.2 Force–displacement response

The force–displacement curves of both tests are shown in Fig. 6. Since hydraulic jacks are controlled by an imposed displacement, the force measured by each actuator is slightly variable for the same displacement due to the variability of material properties in the beam, and the potential small asymmetry in the force introduction positions. The average maximum force obtained between the 2 actuators is 218 kN. The beam has an elastic behavior up to 100 kN (Sect. 4.2), followed by a hardening behavior until the maximum force is reached, while the softening response is characterized by a rapid decrease of the resisting force. The structure nonetheless shows an important capacity of deformation in the post-peak domain.

The maximum force recorded during the experiment agrees with the estimation of the analytical model ($Q_{\max,th} = 204$ kN), with a difference of 6.8%. The analytical model is thus validated. This maximum force is significantly larger than the design service loading (by 360%) and design ultimate resistance (by 160%), showing that the design was conservative. Results of this experimental campaign have confirmed the expected ductile structural behavior.

3.3 Elastic domain

In this chapter, the beam structural behavior under service loading is studied. Five loading–unloading cycles have been performed between the self-weight load level ($F = 20$ kN) and the live-load level for the serviceability limit state ($F = 60$ kN) related to the actual bridge trough, which corresponds to the stress in the transverse beam when heavy train axles cross the bridge. The force–displacement responses, measured with the LVDT sensors, show a hysterical behavior of the beam during these loading cycles (Fig. 7a). This result is confirmed by the measurements of the force–deformation responses of the extensometers (Fig. 7b). The slope of force–displacement responses differs between extensometers due to their location on the beam (Fig. 5).

For all the measurements, the behavior of the beam is observed to be elastic. This result validates that the structural behavior of the beam is adapted to the service conditions. The structural design is thus appropriate. In the following sections, an in-depth analysis of the failure mode is performed.



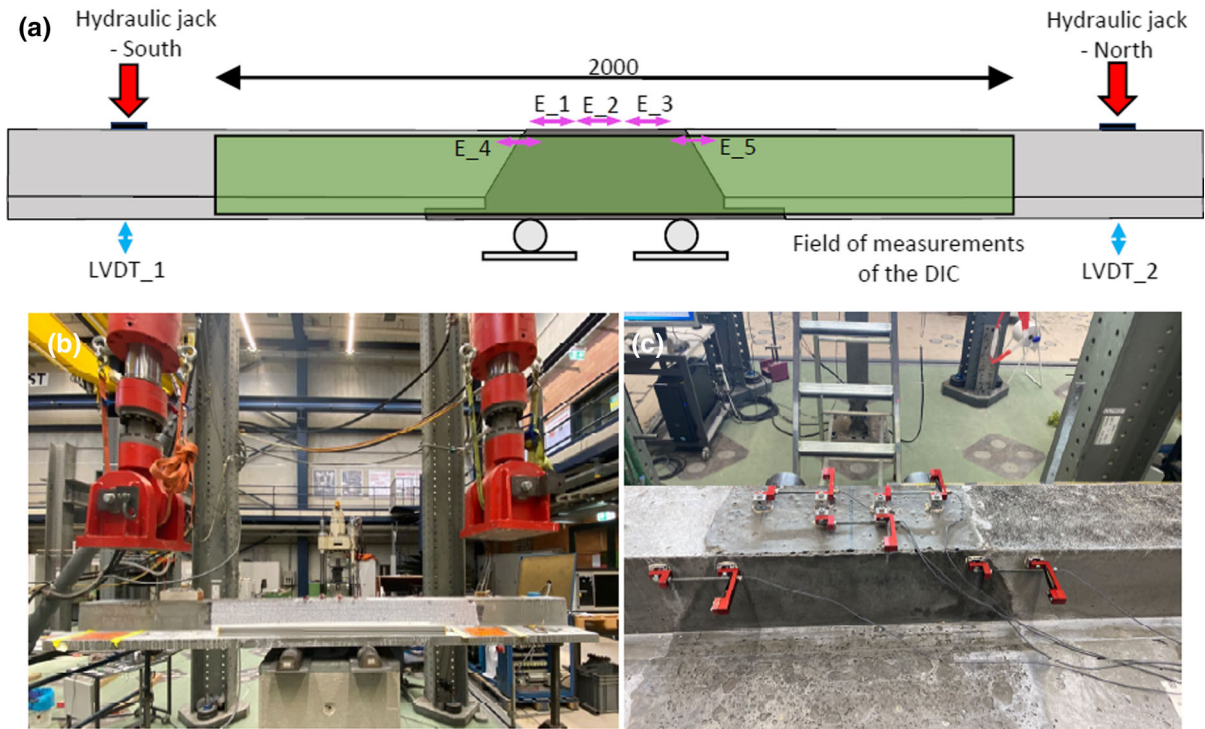
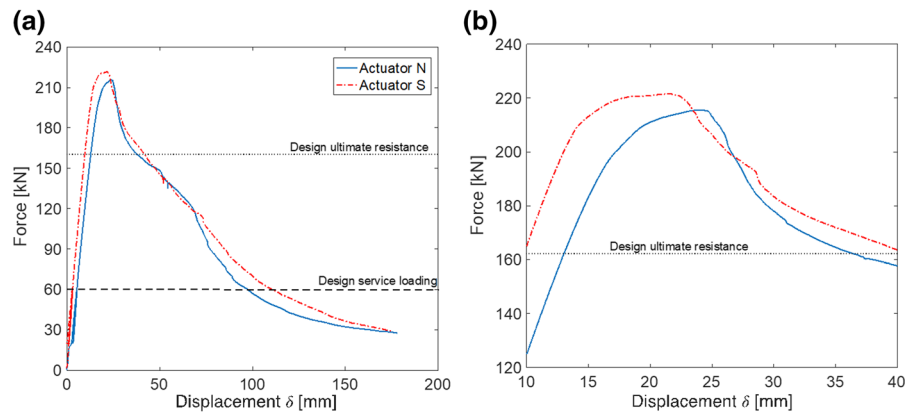


Fig. 5 Experimental setup. **a** Scheme of the experiment; **b** Photograph of the test set up. **c** Locations of the extensometers

Fig. 6 **a** Force–displacement response. **b** zoom in the response near the peak force



3.4 Keying-joint behavior

3.4.1 Cracking patterns

In this Section, the cracking patterns are analyzed using DIC measurements. These measurements enable the evaluation of the deformation of the entire beam over a given area. These measurements are made only on one side of the beam. As rebars had to be placed asymmetrically in the keying joint to avoid conflicting

rebars (Fig. 3), asymmetrical cracking patterns have been observed between the two sides of the beam.

Figure 8 presents results obtained with the DIC for several force–displacement points, using the force results of Actuator S (Fig. 6). In these graphs, the color differences show the gradient of deformation. At the service load conditions (Fig. 8a), a small crack is detected by the DIC at the interface between the joint and the precast elements (between green and yellow areas). Although small deformations are observed

Fig. 7 Structural behavior under loading–unloading cycles of service conditions. **a** Force–displacement response; **b** Force–strain response

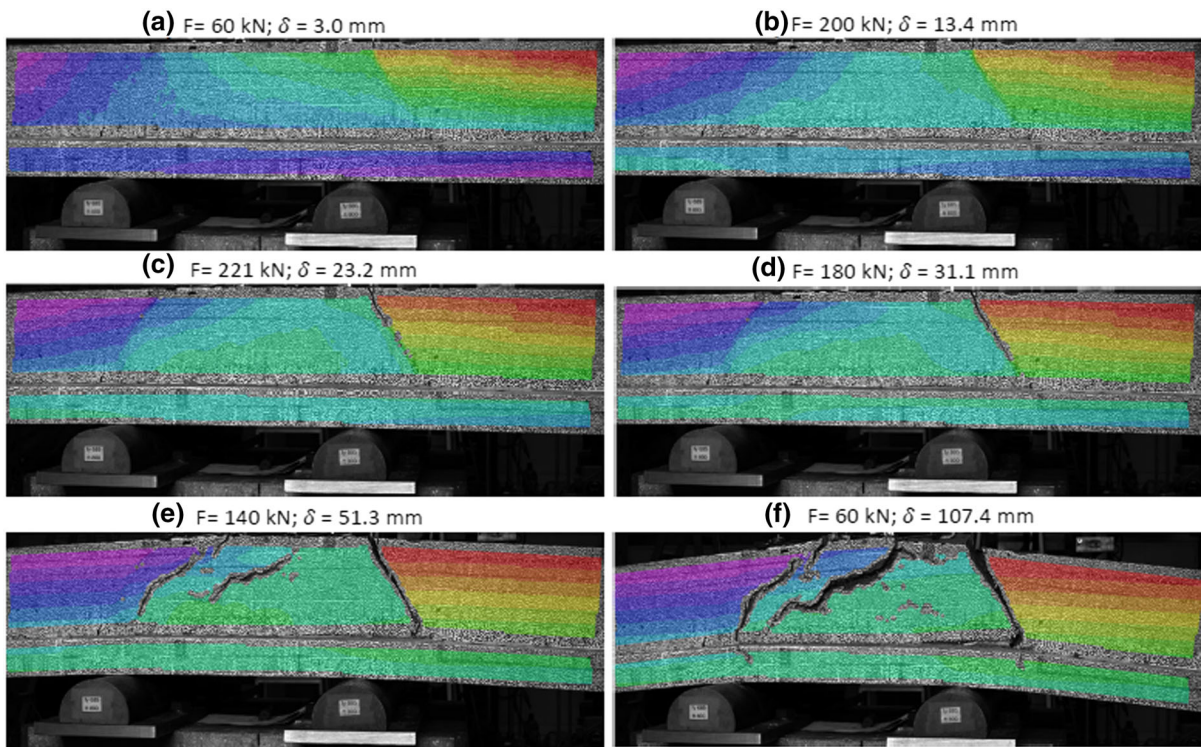
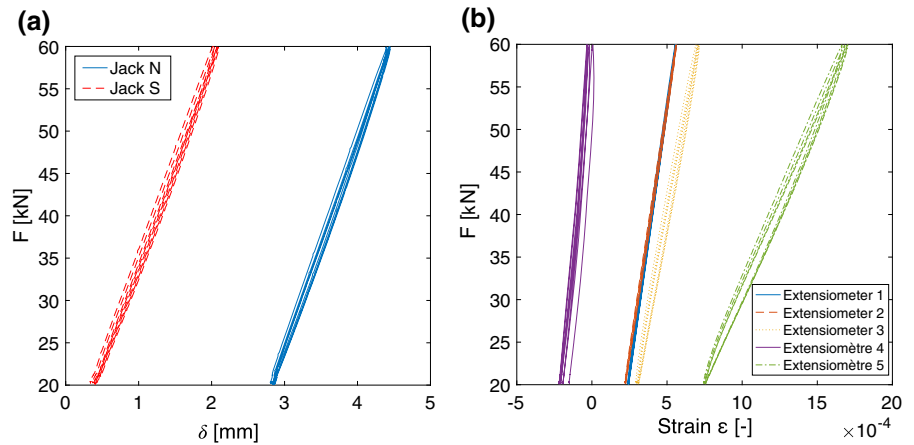


Fig. 8 Cracking patterns observed with the digital image correlation (DIC) system. The First cracks appear exactly at the interface of the keying joint with precast elements

until $F = 200$ kN (Fig. 8b), no crack with a width larger than 0.02 mm is observed on the beam. At the maximum force (Fig. 8c), the 1st crack appears directly on the joint location with a maximum opening of 2 mm. Then, this crack continues to develop when increasing the imposed displacement on the beam. Next, a second crack starts on the opposite joint (Fig. 8d). A 3rd large crack eventually develops in the

main section (Fig. 8d, e). This cracking pattern validates the hypothesis that the interfaces between the keying joint and the precast elements are the weakest section of the beam, and thus determine the ultimate resistance of the structural element.

A more comprehensive study of the 1st crack development is presented in Fig. 9. Under service condition ($F = 60$ kN), the crack is not visible by

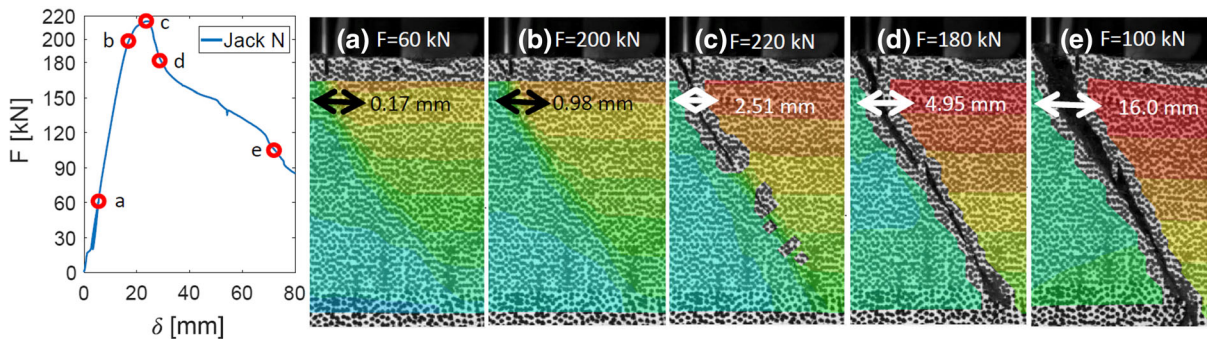


Fig. 9 Keying-joint cracking with respect to the force–displacement response. The crack starts to develop at the maximum force

naked eyes, but is detected by the DIC and highlighted by a change of color on the keying-joint interface. The crack becomes more and more visible on DIC results until $F = 200$ kN, showing an increase of the crack opening with the increase of the loading. At the peak ($F = 220$ kN), the crack with an opening of 2.5 mm is visible with naked eyes and identified by the DIC. Then, this crack continues to develop and open when increasing the imposed displacement of the beam.

The development of this macrocrack coincides with the maximum force on the beam, showing that it governs the global behavior of the beam. Additionally, the opening of this crack leads to a significant increase in the displacement measured during the 4-point bending due to the rotation of the cantilever precast elements.

3.4.2 Crack opening

In this section, a detailed analysis of the crack opening at the interface between the keying joint and the precast elements is made based on the DIC measurements. The crack is measured at the top area of DIC measurements that correspond to the vertical position of the top layer of steel reinforcement in the beam (Fig. 3).

Two inflection points are observed in the crack opening measurements over time using the DIC. The first inflection point approximatively corresponds to the maximum force, while the second inflection point coincides with a significant drop of the force (Fig. 10a). These results confirm that the force is governed by the development of the crack at the interface of the keying joint and precast element.

When comparing the vertical displacement of the beam and the crack opening (Fig. 10b), both responses

over time are similar. This result shows that the displacement of the beam is mainly governed in the post-peak domain by the crack at both interfaces.

Figure 11 presents a comparison of the force–crack opening and force–displacement responses close to the maximum force. Both the DIC and extensometer (S5, Fig. 5) are used to record the crack openings on both interfaces between the keying joint and precast elements. These measurements are shown with respect to the force at the actuator on the corresponding side. Measurements of the crack opening show a sharp inflection of slope almost at the maximum force, while the transition is smoother in the force–displacement curve. This result shows that the crack suddenly opens and stops the force increase.

The crack opening is also measured during the loading–unloading cycles of service conditions (Fig. 12) by the DIC. The crack at the interface between the keying joint and precast element on top of the beam has an opening between 0.1 (self-weight) and 0.2 mm (service loading). The crack opening follows the loading–unloading cycles and does not increase between cycles. This result shows that the crack developed during the first loading and then remained stable under service conditions.

3.5 Collapse mechanism

Once the test is performed, the collapse mechanism of the beam is studied (Fig. 13). In the 1st and 2nd photographs (Fig. 13a, b), the collapse mechanism largely in the post-peak domain at the end of the test is observed. Two plastic hinges have been created on the interface between the keying joint and the precast elements, showing that these interfaces are the weakest points on the beam. These hinges lead to a

Fig. 10 Crack opening over time with respect to **a** force–time response and **b** vertical displacement–time response

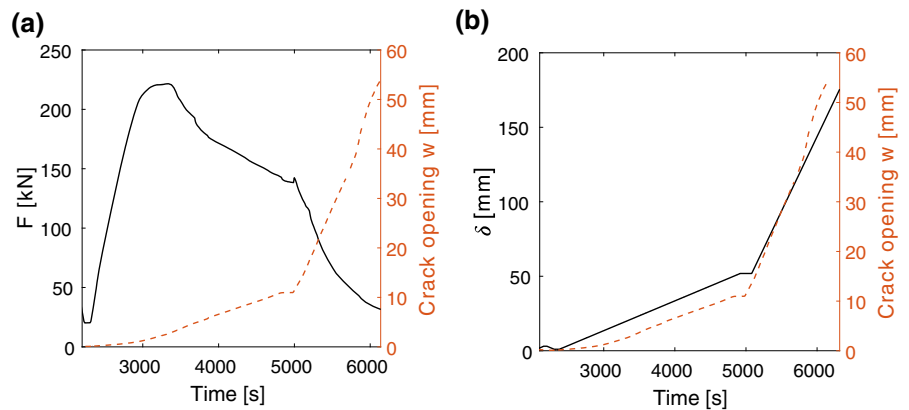


Fig. 11 Structural behavior close to the maximum force. **a** Force–crack opening response; **b** Force–displacement response

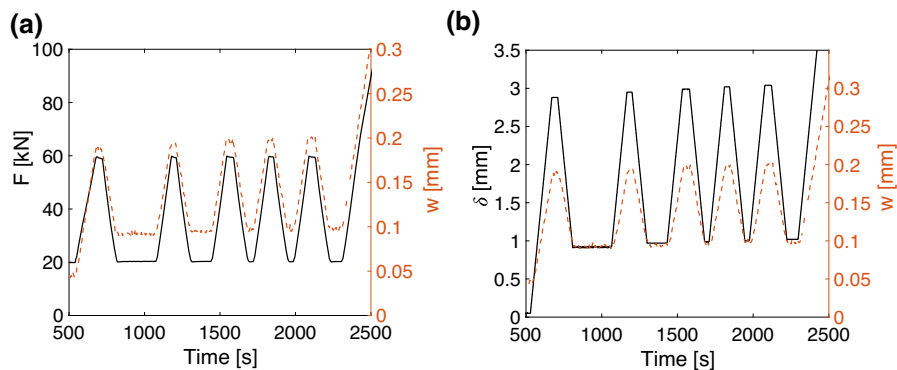
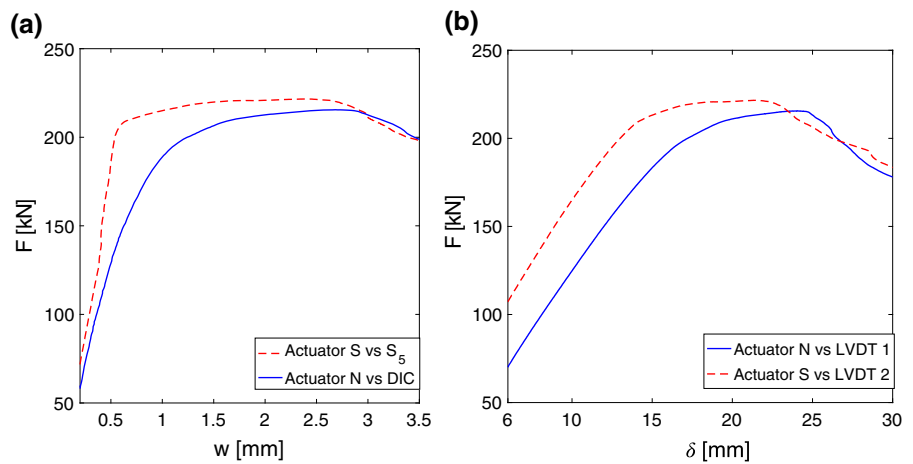


Fig. 12 Crack opening over time in the elastic domain with respect to **a** force–time response and **b** vertical displacement–time response

confinement of the UHPFRC in the keying joint. In the third photograph (Fig. 13c), it can be seen that the reinforcing bars did not reach yielding. The rupture thus occurred by pulling out of the reinforcement bars.

This rupture mechanism does not affect the ductility of the structural behavior (Fig. 6). Due to the high

compressive and tensile strengths, splitting fracture of UHPFRC did not occur, leading to the significant ductility of the failure mode. This result is in agreement with [34] that have shown that the high Fibre content of UHPFRC (3 volume-%) significantly

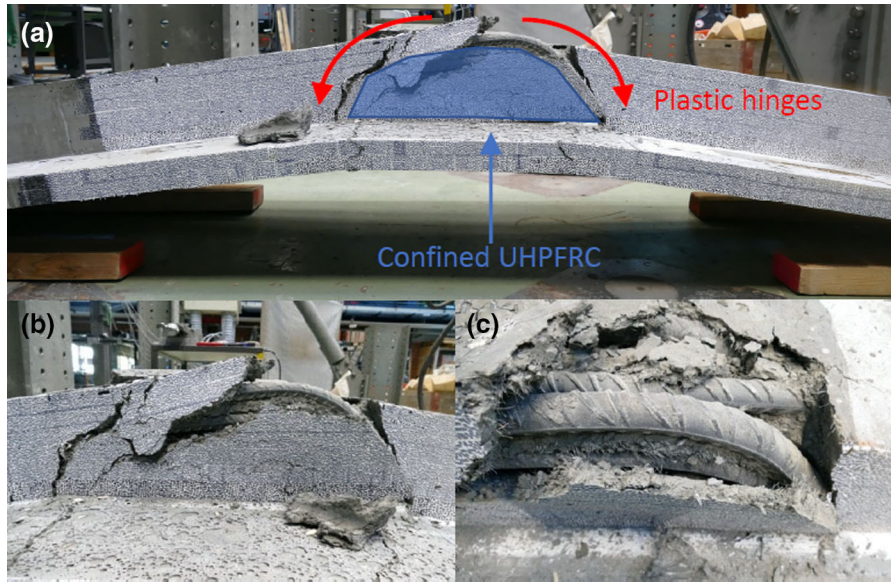


Fig. 13 Beam collapse mechanism after the test. **a** Plastic hinges formation with a UHPFRC confinement; **b** Bursting of the embedding UHPFRC **c** pullout of rebars without yielding

improves the bond strength and allows to anchor rebars in thin UHPFRC layers.

4 Inverse analysis of beam properties

4.1 Observed beam rigidity

In this section, an inverse analysis is performed to obtain beam properties. The first analysis involves determining the beam rigidity based on its observed deformation in the elastic domain. In a 4-point bending test, the rigidity of the beam is obtained using Eq. 1 with respect to the difference of stress (ΔP) and displacement ($\Delta \delta$) and geometric characteristics: the length of the beam ($l = 2400$ mm), the distance between the force and the support ($a = 1000$ mm) and the beam inertia ($I = 3.54E8$ mm⁴). The results of the loading–unloading cycles (Fig. 7) are taken for the inverse analysis ($\Delta P = 40$ kN; $\Delta \delta \cong 1.67$ mm).

$$EI = \frac{1}{6} \frac{\Delta P}{\Delta \delta} a (3 * l * a - 4 * a^2) \quad (1)$$

The calculated rigidity is equal to $1.28 * 10^{13}$ Nmm². Using Young's modulus of UHPFRC (Table 1) and the hypothesis on an uncracked section, the theoretical stiffness of the

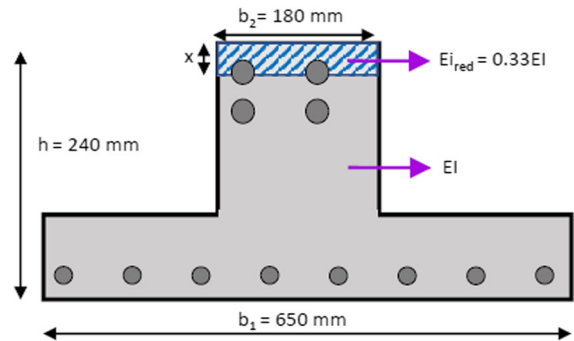


Fig. 14 Model of the beam stiffness

beam is equal to $1.59 * 10^{13}$ Nmm², meaning that the theoretical stiffness is 20% higher than the observed value. This result confirms the hardening behavior of the UHPFRC in the tensile side of the beam.

UHPFRC beam is assumed to have a reduced stiffness in the tensile side as the UHPFRC has a Young's modulus value that is 67% smaller in the hardening domain (Fig. 14). By minimizing the difference between calculated and observed beam stiffness, the height of the UHPFRC-hardening area is estimated to $x = 30$ mm with an average UHPFRC deformation of 0.1%. The UHPFRC is hardening until the first rebar layer (Fig. 3).

4.2 Evaluation of the ductility of structural behavior

Another goal of the test is to observe the post-peak behavior of the structure to ensure that the collapse mechanism shows significant deformation capacity. A deformation-based measure of ductility has been introduced for concrete beams [35, 36]. The ductility of the structure μ_E is calculated using Eq. 2, where δ_{el} is the elastic deformation, δ_U is the deformation at the maximum force, M_{el} is the bending moment at the end of the elastic domain and M_U is the maximal bending-moment capacity of the structure.

$$\mu_E = \frac{\delta_U}{\delta_{el}} * \frac{M_U}{M_{el}} \quad (2)$$

Considering the non-linear behavior of UHPFRC, the end of the linearity of the force–deformation curve is defined by a difference of 10% between the apparent secant beam rigidity E_i (Eq. 3) and its moving average over 20 periods, following recommendations in [16, 37].

$$EI_i = \frac{1}{6} \frac{P_i}{\delta_i} a (3 * l * a - 4 * a^2) \quad (3)$$

In the present study, the elastic limit is calculated using the force–displacement responses (Fig. 6), and the ductility coefficient is then evaluated for each actuator force. The evaluation of the ductility is then taken as the average value (Table 3). Compared to a R-UHPFRC beam made of a single element, the ductility of the beam in the present study is lower, but values are in the same order of magnitudes. This result confirms that the beam presented in this study has an important capacity of deformation even if the fibers are not continuous through the element. This result confirms the validity of the flexural-behavior model presented in Sect. 2.3.

Table 3 Comparison of ductility evaluation between the present study and conventional RC beams and a R-UHPFRC beam made of a single element

Ductility capacity evaluation	Present study	R-UHPFRC beam [16]
μ_E	6.9	10

4.3 Stress in rebars

The second inverse analysis involves determining the stress level in the rebars. Two methods are used to infer the rebar stress based on deformation measurements using DIC and extensometers.

The stress is first calculated based on the deformation measured by the DIC at the location of the rebar on the uncracked area. Then, the rebar stress is inferred from this deformation using Hooke's law. A similar procedure is then used to infer the stress in the reinforcement bar based on the extensometer measurements at the rebar location. The extensometer located on the uncracked area is used (E4, Fig. 5). Although these deformation measurements are made on the UHPFRC surface, it is assumed that the deformation of the steel is similar as the cover of rebars is only 15 mm. Nonetheless, these stress estimations are only valid when the beam exhibits an elastic behavior.

The 2 estimations of the rebar stress are compared in Fig. 15. Both stress estimations are similar. In the loading–unloading cycles, these estimations correspond to the steel level expected in the elastic domain (150 MPa). When increasing the force to the maximum value, the maximum measured stress is close to 550 MPa, which is slightly higher than the nominal yielding stress of steel (500 MPa) and a stress level expected under this loading condition. As both methods provide similar results and are in agreement with the analytical models, the proposed approach to assess steel stresses in the rebar with indirect measurements of the DIC and extensometers is validated.

5 Conclusions

This paper presents a full-scale experimental investigation of a keying joint between precast elements all made of UHPFRC. A 4-point bending test was performed until the collapse of the beam. Measurements were collected using LVDTs, extensometers, and DIC. The following conclusions can be drawn based on the experimental investigation:

- Results of this laboratory campaign have confirmed the expected structural behavior of this particular beam design and show that the design was highly conservative.

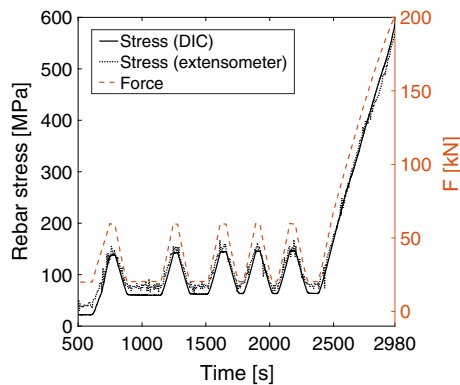


Fig. 15 Stress rebars calculated with DIC and extensometers measurements over time with respect to the force–time response

- The keying joint made of UHPFRC has exhibited a significant ductility in the hardening domain and an important capacity of deformation in the softening domain even if the collapse mechanism was linked to the bond-slip of rebars within the joint.
- Under service conditions, the structure has an elastic structural behavior even if cracks at the interface of the precast elements and the poured UHPFRC are detected by the DIC.
- The study of the cracking patterns shows that the cracks develop at the interface between the keying joint and the precast elements. The crack opening suddenly increases when the load condition is near the peak.

Future works consist in the modeling of the structural behavior using finite-element models to better predict the keying-joint behavior and crack development.

Acknowledgements The authors are thankful to Dr. B. Sawicki for his valuable inputs.

Authors contribution All authors contributed to the study conception and design. Material preparation, data collection and analysis were performed by NJB and EB. Conception of the bridge was made by NTT, EG and EB. The first draft of the manuscript was written by NJB and all authors commented on previous versions of the manuscript. All authors read and approved the final manuscript.

Funding Open access funding provided by EPFL Lausanne. No funding was received for conducting this study.

Declarations

Conflict of interest The authors have no relevant financial or non-financial interests to disclose.

Open Access This article is licensed under a Creative Commons Attribution 4.0 International License, which permits use, sharing, adaptation, distribution and reproduction in any medium or format, as long as you give appropriate credit to the original author(s) and the source, provide a link to the Creative Commons licence, and indicate if changes were made. The images or other third party material in this article are included in the article's Creative Commons licence, unless indicated otherwise in a credit line to the material. If material is not included in the article's Creative Commons licence and your intended use is not permitted by statutory regulation or exceeds the permitted use, you will need to obtain permission directly from the copyright holder. To view a copy of this licence, visit <http://creativecommons.org/licenses/by/4.0/>.

References

1. Frangopol DM, Liu M (2007) Maintenance and management of civil infrastructure based on condition, safety, optimization, and life-cycle cost*. *Struct Infrastruct Eng* 3:29–41. <https://doi.org/10.1080/15732470500253164>
2. Bocchini P, Frangopol D, Ummenhofer T, Zinke T (2014) Resilience and sustainability of civil infrastructure: toward a unified approach. *J Infrastruct Syst* 20:04014004
3. Pamenter S, Myers RJ (2021) Decarbonizing the cementitious materials cycle: a whole-systems review of measures to decarbonize the cement supply chain in the UK and European contexts. *J Ind Ecol* 25:359–376. <https://doi.org/10.1111/jiec.13105>
4. Azmee NM, Shafiq N (2018) Ultra-high performance concrete: from fundamental to applications. *Case Stud Constr Mater* 9:e00197. <https://doi.org/10.1016/j.cscm.2018.e00197>
5. Graybeal B, Brühwiler E, Kim B-S et al (2020) International perspective on UHPC in bridge engineering. *J Bridge Eng* 25:04020094. [https://doi.org/10.1061/\(ASCE\)BE.1943-5592.0001630](https://doi.org/10.1061/(ASCE)BE.1943-5592.0001630)
6. Brühwiler E, Denarié E (2013) Rehabilitation and strengthening of concrete structures using ultra-high performance fibre reinforced concrete. *Struct Eng Int* 23:450–457. <https://doi.org/10.2749/101686613X13627347100437>
7. Brühwiler E (2016) “Structural UHPFRC”: welcome to the post-concrete era! International interactive symposium on ultra-high performance concrete. Iowa State University Digital Press, Des Moines, Iowa, pp 1–16
8. Brühwiler E (2020) UHPFRC technology to enhance the performance of existing concrete bridges. *Struct Infrastruct Eng* 16:94–105. <https://doi.org/10.1080/15732479.2019.1605395>
9. Yoo D-Y, Yoon Y-S (2016) A review on structural behavior, design, and application of ultra-high-performance fiber-reinforced concrete. *Int J Concr Struct Mater* 10:125–142. <https://doi.org/10.1007/s40069-016-0143-x>

10. Oesterlee C (2010) Structural response of reinforced UHPFRC and RC composite members. EPFL, Lausanne
11. Abdel M (2019) Simplified design approach of steel fiber reinforced concrete under flexural load. In: Proceedings of the 10th international conference on fracture mechanics of concrete and concrete structures. IA-FraMCoS
12. Farhat FA, Nicolaides D, Kanellopoulos A, Karihaloo BL (2007) High performance fibre-reinforced cementitious composite (CARDIFRC)–Performance and application to retrofitting. *Eng Fract Mech* 74:151–167. <https://doi.org/10.1016/j.engfracmech.2006.01.023>
13. Qiu M, Shao X, Wille K et al (2020) Experimental investigation on flexural behavior of reinforced ultra high performance concrete low-profile T-beams. *Int J Concr Struct Mater* 14:5. <https://doi.org/10.1186/s40069-019-0380-x>
14. Huang B-T, Li Q-H, Xu S-L, Zhang L (2019) Static and fatigue performance of reinforced concrete beam strengthened with strain-hardening fiber-reinforced cementitious composite. *Eng Struct* 199:109576. <https://doi.org/10.1016/j.engstruct.2019.109576>
15. Yang I-H, Joh C, Bui TQ (2019) Estimating the tensile strength of ultrahigh-performance fiber-reinforced concrete beams. *Adv Mater Sci Eng* 2019:1–16. <https://doi.org/10.1155/2019/5128029>
16. Sawicki B, Brühwiler E, Denarié E (2020) Inverse analysis of R-UHPFRC members to determine the flexural response underservice loading and at ultimate resistance. *J Struct Eng* 148:040221260
17. Swiss Society of Engineers and Architects (2016) Technical leaflet on UHPFRC: materials, design and application
18. Brühwiler E (2018) Structural UHPFRC to enhance bridges. In: Proceedings of the 2nd international conference on UHPC materials and structures UHPC. Fuzhou, pp 140–158
19. Charron J-P, Denarié E, Brühwiler E (2007) Permeability of ultra high performance fiber reinforced concretes (UHPFRC) under high stresses. *Mater Struct* 40:269–277. <https://doi.org/10.1617/s11527-006-9105-0>
20. Paul SC, van Zijl GP, Šavija B (2020) Effect of fibers on durability of concrete: a practical review. *Materials* 13:4562
21. Denarié E, Brühwiler E (2015) Cast-on site UHPFRC for improvement of existing structures—achievements over the last 10 years in practice and research. RILEM Publication SARL, Marne-la-Vallée
22. Toutlemonde F, ROENELLE P, Hajar Z, et al (2013) Long-term material performance checked on world's oldest UHPFRC road bridges at Bourg-Lès-Valence. RILEM Publication SARL, Marne-la-Vallée, pp 265–274
23. Bertola N, Küpfer C, Kálin E, Brühwiler E (2021) Assessment of the environmental impacts of bridge designs involving UHPFRC. *Sustainability* 13:12399. <https://doi.org/10.3390/su132212399>
24. Hajiesmaeili A, Pittau F, Denarié E, Habert G (2019) Life cycle analysis of strengthening existing RC structures with R-PE-UHPFRC. *Sustainability* 11:6923. <https://doi.org/10.3390/su11246923>
25. Denarié E, Brühwiler E (2006) Structural rehabilitations with ultra-high performance fibre reinforced concretes (UHPFRC). *Restor Build Monum Bauinstandsetz Bau- denkmalfpflege* 12:453–468
26. Bertola N, Schiltz P, Denarié E, Brühwiler E (2021) A review of the use of UHPFRC in bridge rehabilitation and new construction in Switzerland. *Front Built Environ* 7:155. <https://doi.org/10.3389/fbuil.2021.769686>
27. Nunes S, Pimentel M, Ribeiro F et al (2017) Estimation of the tensile strength of UHPFRC layers based on non-destructive assessment of the fibre content and orientation. *Cem Concr Compos* 83:222–238. <https://doi.org/10.1016/j.cemconcomp.2017.07.019>
28. Bastien-Masse M, Denarié E, Brühwiler E (2016) Effect of fiber orientation on the in-plane tensile response of UHPFRC reinforcement layers. *Cem Concr Compos* 67:111–125. <https://doi.org/10.1016/j.cemconcomp.2016.01.001>
29. Shen X, Brühwiler E, Peng W (2020) Biaxial flexural response of strain-hardening UHPFRC circular slab elements. *Constr Build Mater* 255:119344. <https://doi.org/10.1016/j.conbuildmat.2020.119344>
30. Makita T, Brühwiler E (2014) Tensile fatigue behaviour of ultra-high performance fibre reinforced concrete combined with steel rebars (R-UHPFRC). *Int J Fatigue* 59:145–152. <https://doi.org/10.1016/j.ijfatigue.2013.09.004>
31. Sawicki B, Brühwiler E, Bassil A (2021) Deformational behavior and damage mechanism of R-UHPFRC beam subjected to fatigue loading. *Mater Struct* 54:158. <https://doi.org/10.1617/s11527-021-01745-3>
32. Sawicki B, Brühwiler E (2021) Fatigue resistance of reinforced UHPFRC beams. *Int J Fatigue* 148:106216. <https://doi.org/10.1016/j.ijfatigue.2021.106216>
33. Peng K, Yan B (2022) Experimental study of the flexural behaviour of ultra-high-performance concrete beam with wet joint. *Mag Concr Res* 74:70–80. <https://doi.org/10.1680/jmacr.20.00078>
34. Oesterlee C, Sadouki H, Brühwiler E (2008) Structural analysis of a composite bridge structure combining UHPFRC and prestressed concrete, vol 104, *Beton-und Stahlbetonbau*, pp 462–470
35. Jaeger LG, Mufti AA, Tadros G (1997) The concept of the overall performance factor in rectangular-section reinforced concrete members. In: Proceedings of the 3rd international symposium on non-metallic (FRP) reinforcement for concrete structures. Sapporo, pp 551–559
36. Wang H, Belarbi A (2011) Ductility characteristics of fiber-reinforced-concrete beams reinforced with FRP rebars. *Constr Build Mater* 25:2391–2401. <https://doi.org/10.1016/j.conbuildmat.2010.11.040>
37. Denarié E, Sofia L, Brühwiler E (2017) Characterization of the tensile response of strain hardening UHPFRC-Chillon viaducts. In: Proceedings AFGC-ACI-fib-RILEM Int. Symposium on ultra-high performance fibre-reinforced concrete, UHPFRC 2017-Pro 106. RILEM publications S.A.R.L., Montpellier, pp 242–250

Publisher's Note Springer Nature remains neutral with regard to jurisdictional claims in published maps and institutional affiliations.

